# $O(^3P_J)$ Formation and Desorption by 157-nm Photoirradiation of Amorphous Solid Water

Alice J. DeSimone – Georgia Institute of Technology
Thomas M. Orlando – Georgia Institute of Technology



Citation of published version:

DeSimone, A., Orlando, T. (2014): $O(^3P_J)$ Formation and Desorption by 157-nm Photoirradiation of Amorphous Solid Water. *The Journal of Chemical Physics*, 140.
DOI: https://doi.org/10.1063/1.4867194

# $O(^3P_J)$ formation and desorption by 157-nm photoirradiation of amorphous solid water

Alice J. DeSimone, and Thomas M. Orlando

Citation: The Journal of Chemical Physics **140**, 094702 (2014); doi: 10.1063/1.4867194
View online: https://doi.org/10.1063/1.4867194
View Table of Contents: http://aip.scitation.org/toc/jcp/140/9
Published by the American Institute of Physics

# $O(^3P_J)$ formation and desorption by 157-nm photoirradiation of amorphous solid water

Alice J. DeSimone[1] and Thomas M. Orlando[1,2,a)]
[1]*School of Chemistry and Biochemistry, Georgia Institute of Technology, Atlanta, Georgia 30332–0400, USA*
[2]*School of Physics, Georgia Institute of Technology, Atlanta, Georgia 30332–0400, USA*

(Received 29 October 2013; accepted 17 February 2014; published online 6 March 2014)

Photodissociation of amorphous solid water (ASW) deposited on a thinly oxidized copper substrate at 82 K was studied by measuring $O(^3P_{J=2,1,0})$ photoproducts detected with resonance-enhanced multiphoton ionization. For each spin-orbit state, the oxygen atom time-of-flight spectrum was measured as a function of $H_2O$ exposure, which is related to ice thickness, and 157-nm irradiation time. Four Maxwell-Boltzmann distributions with translational temperatures of 10 000 K, 1800 K, 400 K, and 82 K were found to fit the data. The most likely formation mechanisms are molecular elimination following ionization of water and ion-electron recombination, secondary recombination of hydroxyl radicals, and photodissociation of adsorbed hydroxyl radicals. Evidence for O-atom diffusion through bulk ASW was found for $H_2O$ exposures of at least 5 Langmuir (1 L = $10^{-6}$ Torr s). The cross sections for $O(^3P_2)$ depletion were $1.3 \times 10^{-19}$ and $6.5 \times 10^{-20}$ cm$^2$ for 1 and 5 L, respectively. © *2014 AIP Publishing LLC*. [http://dx.doi.org/10.1063/1.4867194]

## I. INTRODUCTION

Oxygen atoms, which may be produced by photodissociation of water, have been observed in several exospheres within our solar system.[1] The neutral clouds around Saturn, containing $H_2O$, OH, and O, are thought to originate from water ice on Enceladus.[2,3] Hydroxyls were first detected in Saturn's magnetosphere by the Faint Object Spectrograph on the Hubble Space Telescope.[4] Since then, an atomic oxygen cloud has been observed that is even broader than the OH cloud.[5] Models of the neutral cloud coming from Enceladus include losses due to charge exchange, dissociation, and ionization of $H_2O$, OH, and O.[6] Therefore, it is important to examine the yields of atomic fragments due to photodissociation of water. Neutral-neutral collisions within the cloud are also included in recent models to account for some of its outward spreading.[7] Although only gas-phase interactions are generally included in models, condensed-phase processes may also be important in the neutral cloud, particularly in the E ring, since geysers on Enceladus can release ice-covered grains into the E ring.[8] When an icy grain surface is involved, $H_2O$ and O may be formed by recombination of OH radicals produced by dissociation of electronically excited $H_2O$. This recombination reaction is one of the primary mechanisms of $O(^3P_J)$ formation and release discussed in the present work.

In a recent paper, we investigated the photodesorption of intact $H_2O$ molecules from amorphous solid water (ASW).[9] We focused on the nature of the first excited state of water, which is dissociative in the gas phase but may lead to desorption in the condensed phase due to exciton diffusion. Exciton diffusion is in competition with direct dissociation into reactive H, O, and OH fragments,[10] and the yields of these photoproducts are essential to understanding the relative significances of photodesorption and photodissociation of water.

Because photodissociation of water is such an important process in atmospheric, interstellar, and planetary chemistry, it has been studied extensively.[11–16] Even when the primary experimental goal is to measure photodesorption of water, a significant amount of photodissociation occurs and complicates the interpretation of measured water removal cross sections.[9,17,18] $O(^3P_J)$ formation by 157-nm irradiation of 1500 L amorphous solid ASW at 90 K has been measured previously by Hama *et al.*, who found that four Maxwell-Boltzmann components with translational temperatures of 5000, 1300, 300, and 100 K fit their data.[11] The 5000 K component, which was attributed to hydroxyl dissociation, increased significantly with 30 min of prior irradiation when compared to freshly dosed ASW.[11] When compared to the time-of-flight (TOF) spectrum of $O(^3P_J)$ from ASW, the TOF spectrum for $O(^3P_J)$ from $H_2O_2$ was found to be roughly the same shape but twice as intense.[11] This result lends credence to the idea that most of the $O(^3P_J)$ desorbing from ASW is indirectly formed by hydroxyl radicals, since twice as many hydroxyls are formed during irradiation of $H_2O_2$. Though several different hydroxyl recombination mechanisms may account for the three slowest translational temperature components, no attempt was made to assign individual components to these different pathways, and no cross sections for $O(^3P_J)$ depletion have been reported.[11] The present study examines the pathways of photo-induced formation and release of $O(^3P_J)$ from ASW with well-resolved TOF measurements, extracts cross sections for $O(^3P_J)$ depletion, further examines the effect of cumulative irradiation, and determines $O(^3P_J)$ spin-orbit temperatures as a function of $H_2O$ coverage. Section II describes the experimental approach and data analysis procedures. Section III presents the measured time-of-flight distributions and spin-orbit temperatures as a function

a)Author to whom correspondence should be addressed. Electronic mail: thomas.orlando@chemistry.gatech.edu

 

of $H_2O$ exposure as well as the $O(^3P_J)$ removal cross sections for 1 and 5 L exposures. Section IV then describes the mechanisms of $O(^3P_J)$ production and discusses the relevance of the data to processing icy grains predominately found in the E-ring system of Saturn. Finally, conclusions are given in Sec. V.

## II. EXPERIMENTAL DETAILS

All experiments were performed in an ultra-high vacuum (UHV) chamber that has been described previously.[9] Briefly, this chamber contains a liquid-nitrogen-cooled sample holder, a time-of-flight mass spectrometer, and a leak valve for admitting water vapor to dose the sample. The chamber's base pressure was $2 \times 10^{-10}$ Torr, and background dosing of $H_2O$ was typically performed at pressures between $10^{-8}$ and $10^{-7}$ Torr. For example, to obtain an exposure of 1 L (1 L = $10^{-6}$ Torr s), the chamber pressure was elevated to $10^{-8}$ Torr for 100 s by allowing water vapor to leak in. Experiments were performed at 82 K, the minimum sample temperature, unless otherwise stated. At temperatures below 90 K, ASW films produced by background dosing exhibit significant porosity,[19] which complicates the relationship between $H_2O$ exposure and ice thickness. At low exposures and coverages, water is known to be adsorbed as clusters. Assuming unit sticking probability and neglecting the porosity and clustering, exposures between 0.1 and 600 L lead to upper limit estimates of ice thickness between 0.1 and 600 monolayers.

The copper substrate was mounted directly on the cooled sample mount and was not sputtered between experiments. Thus, a thin oxide layer is expected to coat the surface. Oxygen impurities on copper surfaces are known to promote dissociative adsorption of water, so this distinction between copper oxide and copper metal is important at low exposures.[20] On CuO (100), water chemisorbs molecularly at low temperatures and only dissociatively adsorbs above 198 K.[21] On $Cu_2O$ (100), about 10% of a monolayer of water is dissociated at 110 K, while adsorption is entirely dissociative at 300 K.[22] In the present study, the temperature of the copper with an oxide overlayer is 82 K, so minimal dissociative adsorption is expected when $H_2O$ exposure is at least 1 L.

Unfocused 157-nm light from an excimer laser (GAM Laser, EX5) entered the chamber through a magnesium fluoride window and struck the sample at a 45° angle. The excimer laser energy was typically 160–180 $\mu J\,cm^{-2}$/pulse. $O(^3P_{J=2,1,0})$ photoproducts were detected with 2 + 1 resonance-enhanced multiphoton ionization (REMPI) via the $O(^3P_J - {}^3P_J)$ transitions at 225.6 − 226.4 nm (see Figure 1).[23] These wavelengths were obtained by frequency doubling the visible output of a Nd:YAG-pumped optical parametric oscillator (Spectra-Physics, MOPO-SL), and the beam was focused to a volume of ∼10 $\mu m^3$. The distance between the surface and the detection region based on careful laser alignment was 3 ± 0.5 mm.

The time between desorption and ionization laser pulses was varied with a delay generator from 0 to 30 $\mu$s. Since this delay time equals the flight time of the atom from the surface to the detection region, this measurement yields the TOF of the neutral desorbate. Control of the delay time also allowed different parts of the desorption plume to be probed. The oxygen peak in each mass spectrum was integrated to obtain the total signal for each time delay, and the resulting graph of signal versus time delay is the TOF spectrum. These measurements were carried out for each spin-orbit state at several $H_2O$ exposures.

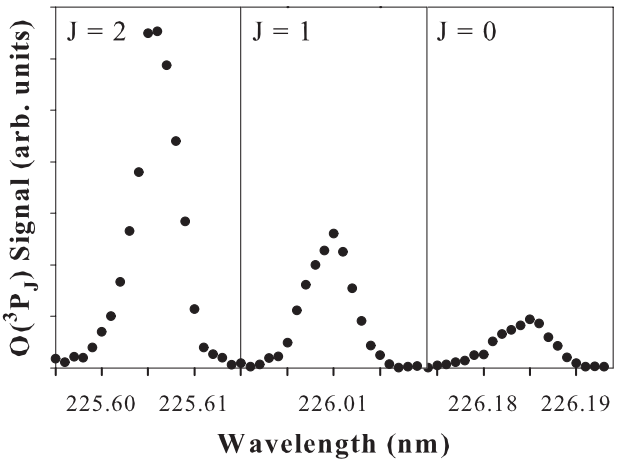


FIG. 1. REMPI spectra of $O(^3P_J)$ desorbing from 600 L ASW at 85 K due to 157-nm irradiation. TOF = 1.4 $\mu$s.

A sum of Maxwell-Boltzmann distributions was used to simulate the TOF spectra.[24] Four Maxwell-Boltzmann components, $S(t, T_{trans})$, were required to adequately fit the experimental data:

$$S(t, T_{trans}) = At^{-4} \exp\left(\frac{-mr^2}{2k_B T_{trans} t^2}\right), \quad (1)$$

where $T_{trans}$ is the translational temperature, $r$ is the distance between the surface and the detection region, and $A$ is a scaling factor. The distance between the surface and the detection region was confirmed to be 3 mm by fitting the thermal component using a Maxwell-Boltzmann distribution with $T_{trans}$ = 82 K.

Using the Jacobian transform, $Pv(v) = tr^2 S(t)$, where $v = r/t$ and $S(t)$ is the measured signal intensity at each time, $O(^3P_J)$ data were also plotted in velocity space. Velocity distributions were fit with Maxwell-Boltzmann components of the form:

$$Pv(v, T_{trans}) = Av^3 \exp\left(\frac{-mv^2}{2k_B T_{trans}}\right), \quad (2)$$

where the values of $T_{trans}$ were those used to fit the TOF spectra and $A$ was a different scaling factor.

Velocity distributions of photodissociation products are expected to follow Maxwell-Boltzmann statistics in strongly quenched systems, when electronic relaxation is fast compared to nuclear motion.[24] In simulated water hexamers, exciton diffusion was found to occur on similar timescales as dissociation of $H_2O$ (∼2 fs),[10] so ASW may have intermediate rather than strong quenching. Nevertheless, Maxwell-Boltzmann distributions are valuable in data interpretation, as

they can reveal various desorption and dissociation channels contributing to observed yields.

## III. RESULTS

Figure 1 shows a representative REMPI spectrum for $O(^3P_J - {}^3P_J)$ transitions due to 157-nm irradiation of 600 L ASW with TOF = 1.4 $\mu$s. The wavelengths shown in Figure 1 are in air, and the corresponding vacuum wavelengths can be found by adding ~0.06 nm. The ratio of the peak areas is 5.9 to 2.4 to 1 for J = 2, 1, and 0.

Generally, to calculate the spin-orbit temperature, one would divide these values by the degeneracy of each state: 5, 3, and 1 for J = 2, 1, and 0, respectively, then plot the natural log of those values versus energy, and finally set the slope equal to $-1/k_B T_{spin\text{-}orbit}$. However, in this case, the shape of the TOF spectrum is different for J = 2, so using only the signal intensity at one flight time does not yield complete information. Instead, integration of the TOF spectrum is required.

Figure 2 shows that the slowest component of the TOF spectrum from 600 L ASW is much larger for J = 2 (the ground state) than for J = 1 or 0. The $O(^3P_0)$ TOF spectrum has been multiplied by 10 so that a direct comparison can be made with the $O(^3P_2)$ spectrum. The $O(^3P_1)$ spectrum has the same shape as the $O(^3P_0)$ spectrum, but it has not been scaled.

The slowest component also disproportionately increased with coverage for J = 2. As shown in Figure 3, 1 L and 50 L $H_2O$ exposure led to very similar spectra, except that the slowest peak was slightly larger for 50 L. While exposures ≥1 L had a very fast component peaked around 0.7 $\mu$s, this peak was not present at 0.1 L.

TOF spectra were also measured for J = 1 and J = 0 at 0.1, 1, 5, 50, and 600 L. All of these TOF spectra were fit with a sum of up to four Maxwell-Boltzmann components calculated using Eq. (1) with $r$ = 3.0 mm and translational temperatures of 10 000 K, 1800 K (allowed to vary between 1600 and 2000 K to get best fit for each scan), 400 K, and 82 K. A sub-thermal, non-Maxwellian component was also observed in some scans at high coverage. Figure 4 shows the 600 L ASW TOF spectrum for J = 2, the four Maxwell-Boltzmann components, and the sum of those components. The error bars represent 95% confidence intervals calculated from many scans after substantial irradiation. After fitting the TOF data with four Maxwell-Boltzmann distributions, the signal that was not fit by their sum at longer flight times was referred to as "the diffusion component." Although Figure 4 only shows data up to 14 $\mu$s, signal was collected out to 30 $\mu$s so that the entire diffusion component could be captured.

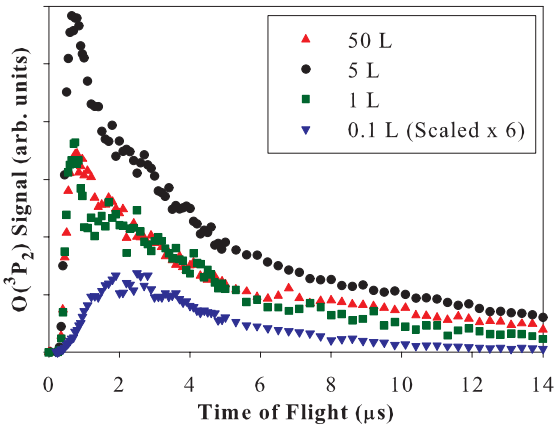


FIG. 3. TOF spectra of $O(^3P_2)$ desorbing from 0.1, 1, 5, and 50 L ASW at 82 K due to 157-nm irradiation.

The corresponding $O(^3P_2)$ velocity distribution from 600 L ASW on copper is shown in Figure 5. Velocities up to 8000 m/s were observed. The most common velocity was 300 m/s, and the second highest peak appeared at 845 m/s. Because of the significant diffusion component, the velocity distribution in Figure 5 could not be used to accurately determine the value of $r$ using the thermal component.

Instead, the value of $r$ was determined using the velocity distribution of $O(^3P_2)$ from a thin layer of ASW deposited on the copper from the background water in the UHV chamber with no intentional dosing (Figure 6). With this extremely low coverage of ASW, no diffusion component was present. Because the 82 K component fit the data best at 3.0 mm, that flight distance was used for all fits. The most common velocities for $O(^3P_2)$ desorbing from a thin layer of ASW background-deposited on copper at 82 K were 600–800 m/s.

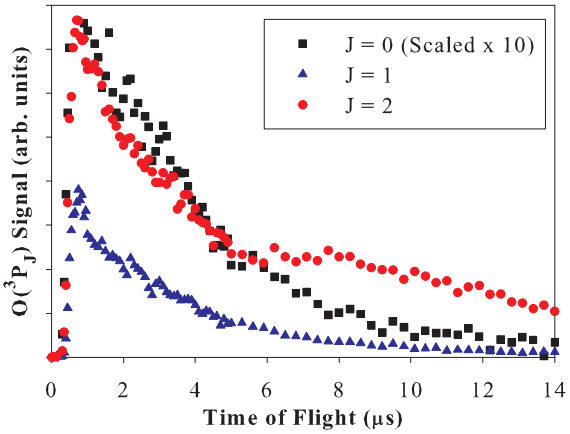


FIG. 2. TOF spectra of $O(^3P_J)$ desorbing from 600 L ASW at 82 K due to 157-nm irradiation.

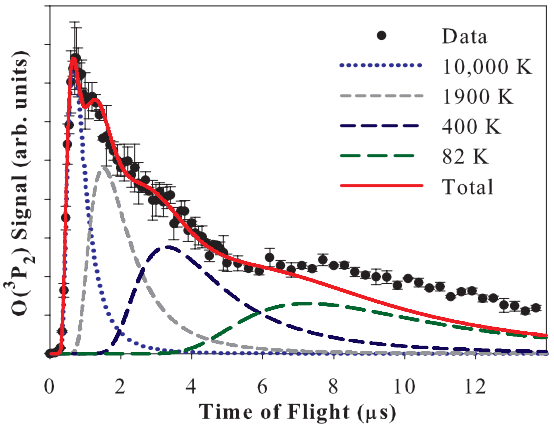


FIG. 4. TOF spectrum of $O(^3P_2)$ desorbing from 600 L ASW at 82 K due to 157-nm irradiation.

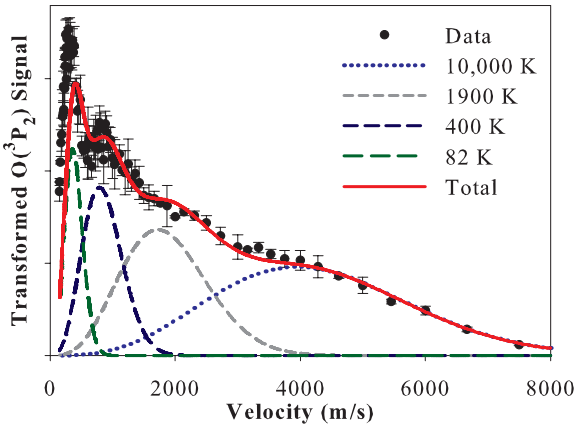


FIG. 5. Velocity distribution of $O(^3P_2)$ desorbing from 600 L ASW at 82 K due to 157-nm irradiation.

The corresponding TOF distribution is shown in Figure 7. Because the $O(^3P_2)$ signal from background-deposited ASW was quite low, some interference occurred from ions produced solely by the excimer laser. The erratic signal around 3 $\mu$s can be explained by this interference. The 10 000 K component was almost unnecessary in fitting the data in Figures 6 and 7.

Table I summarizes the relative yields and component areas for each spin-orbit state at each exposure. The rows labeled "Background" show the percentage of the total TOF area attributed to each Maxwell-Boltzmann component for scans performed without any intentional dosing of water. Therefore, "0.1 L" should be interpreted as 0.1 L on top of the small amount of water deposited during cooling. This amount of unintentional dosing could not be calculated because irradiation during cooling was used to help keep the surface as contaminant-free as possible. The diffusion and thermal components were largest for J = 2. The 5 L, 50 L, and 600 L TOF spectra were very similar to one another for J = 1 and 0. From the relative yields in Table I, the spin-orbit temperatures were calculated to be 1200, 320, 380, 380, and 400 K for 0.1, 1, 5, 50, and 600 L, respectively. The average overall spin-orbit temperature was 543 K, similar to the 600 K spin-orbit

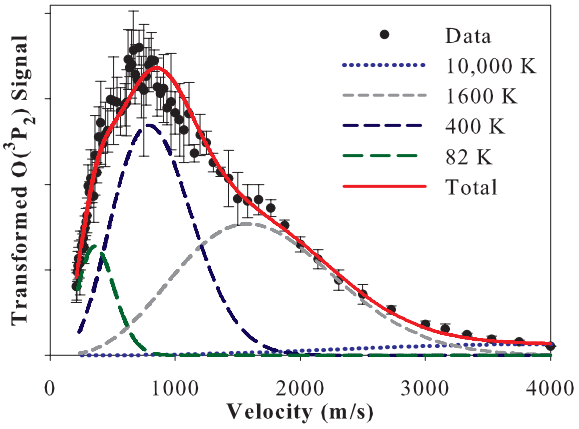


FIG. 6. Velocity distribution of $O(^3P_2)$ desorbing from a thin layer of ASW background-deposited on the oxidized copper substrate at 82 K due to 157-nm irradiation.

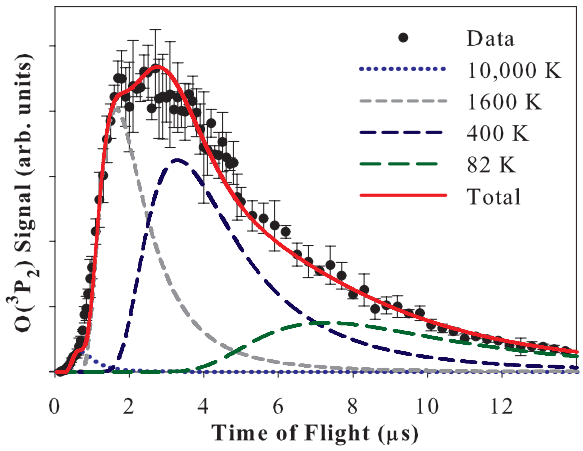


FIG. 7. TOF spectrum of $O(^3P_2)$ desorbing from a thin layer of ASW background-deposited on the oxidized copper substrate at 82 K due to 157-nm irradiation.

temperature reported from 1500 L ASW kept fresh by pulsed dosing.[11]

The spin-orbit temperature reported for 1500 L ASW after 30 min of 157-nm irradiation was 1000 K,[11] and the present study also found significant changes due to increasing irradiation times. The TOF spectra summarized in Table I were measured after the initial period of irradiation during which the signal increases dramatically, as shown in Figure 8. Both $O(^3P_2)$ and $O(^3P_1)$ signals increased much more quickly for the 10 000 K component (TOF = 0.7 $\mu$s) than for the 400 K component (TOF = 3.1 $\mu$s). The 10 000 K component seemed to decrease more quickly than the other components as well, but the difference between components

TABLE I. Relative yields for each $O(^3P_J)$ TOF spectrum and percentages of TOF areas attributed to each Maxwell-Boltzmann or diffusion component.

| | Relative yield | 10 000 K | 1800 K | 400 K | 82 K | Diffusion |
|---|---|---|---|---|---|---|
| | | | J = 0 | | | |
| Background | 1.0 | 1.2 | 31.3 | 59.8 | 7.7 | |
| 0.1 L | 1.0 | 4.5 | 35.4 | 54.9 | 5.2 | |
| 1 L | 3.6 | 24.1 | 20.7 | 46.6 | 8.6 | |
| 5 L | 8.5 | 27.4 | 28.9 | 31.9 | 11.8 | |
| 50 L | 5.2 | 18.4 | 30.1 | 36.2 | 15.3 | |
| 600 L | 5.7 | 24.3 | 27.1 | 37.3 | 11.4 | |
| | | | J = 1 | | | |
| Background | 2.0 | 1.9 | 35.2 | 50.2 | 12.7 | |
| 0.1 L | 2.6 | 2.5 | 40.4 | 46.3 | 10.8 | |
| 1 L | 16.1 | 24.1 | 28 | 39.7 | 8.2 | |
| 5 L | 20.7 | 29.2 | 29.5 | 29.1 | 12.2 | |
| 50 L | 17.2 | 18.2 | 31.3 | 35.9 | 14.6 | |
| 600 L | 16.5 | 24.4 | 29.2 | 33.4 | 13.0 | |
| | | | J = 2 | | | |
| Background | 4.2 | 1.3 | 30.4 | 51.0 | 17.3 | |
| 0.1 L | 6.2 | 2.6 | 36.5 | 47.3 | 13.6 | |
| 1 L | 50.4 | 16.5 | 19.2 | 32.6 | 22.0 | 9.7 |
| 5 L | 90.0 | 14.6 | 18.5 | 26.3 | 22.6 | 18.0 |
| 50 L | 59.4 | 12.7 | 18.4 | 24.0 | 21.2 | 23.7 |
| 600 L | 60.1 | 11.8 | 16.9 | 21.1 | 20.2 | 30.0 |

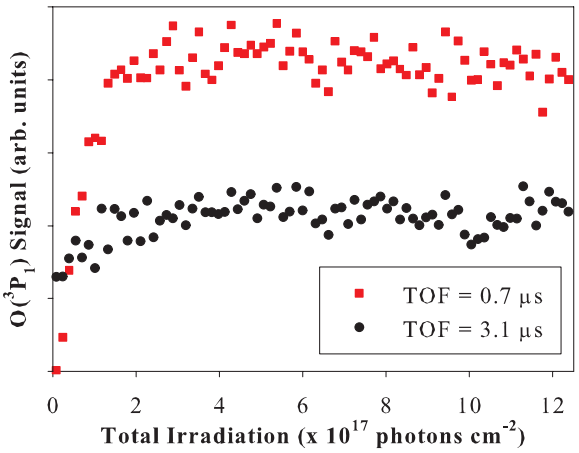


FIG. 8. $O(^3P_1)$ desorbing from 1 L ASW at 82 K as a function of total 157-nm irradiation. Red squares represent the 10 000 K component at TOF = 0.7 $\mu$s, and black circles represent the 400 K component at TOF = 3.1 $\mu$s.

in rate of decrease was minor compared to the difference in rate of increase during initial radiation.

A rapid increase in the 10 000 K component was observed for all exposures ≥1 L. After maximum signal was reached, $O(^3P_J)$ signal remained constant on experimental time scales for 50 L and 600 L. Figure 9 shows the decrease in total $O(^3P_2)$ signal (integrated over time from 0 to 20 $\mu$s) with cumulative irradiation for 1 L and 5 L ASW. In order to determine the cross sections ($\sigma$) for $O(^3P_2)$ depletion, these decreasing signals were fit with exponentials (dashed curves) of the form $y = Ae^{-\sigma x}$, where $x$ has units of photons cm$^{-2}$. The number of 157-nm photons/cm$^2$ was calculated without regard for surface coverage by using the average excimer power and a correction factor of 0.65 for losses passing through the $MgF_2$ window. According to this exponential fitting procedure, the cross sections for $O(^3P_2)$ depletion were $1.3 \times 10^{-19}$ and $6.5 \times 10^{-20}$ cm$^2$ for 1 and 5 L, respectively. For 1 L, total signal increased until ~$4 \times 10^{17}$ photons cm$^{-2}$ (Figure 8). For 5 L, total signal increased for ~$2 \times 10^{18}$ photons cm$^{-2}$, remained approximately constant until $4.5 \times 10^{18}$ photons cm$^{-2}$, and then began to decrease. $O(^3P_2)$ signal increases as hydroxyls accumulate on the surface. Eventually, after five times as many photons as for 1 L, an equilibrium concentration of hydroxyls is reached, and the signal is constant until less than one layer of water remains.

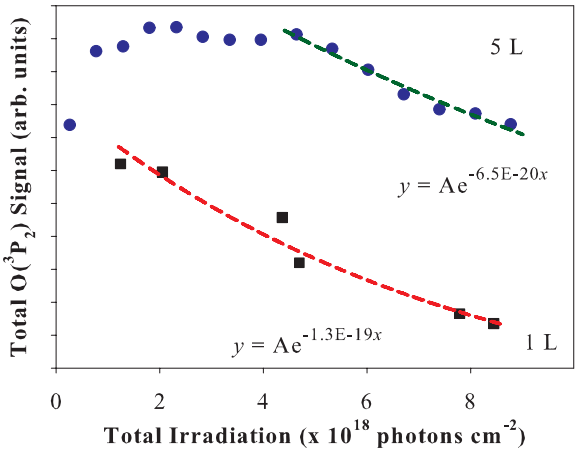


FIG. 9. $O(^3P_2)$ desorbing from 1 L (black squares) and 5 L (blue circles) ASW at 82 K as a function of total 157-nm irradiation. $O(^3P_2)$ TOF spectra were integrated from 0 to 20 $\mu$s to obtain the total signal. The dashed curves represent exponential fits of the form $y = Ae^{-\sigma x}$, where $x$ has units of photons cm$^{-2}$.

## IV. DISCUSSION

### A. $O(^3P_J)$ formation by molecular elimination

$O(^3P_J)$ is a primary product of electron-stimulated dissociation of water ice, which involves a molecular elimination reaction (3) with a threshold of 6–7 eV:[25]

$$H_2O + e^- \rightarrow H_2 + O(^3P_J). \quad (3)$$

The work function of copper is about 4.2–4.7 eV, and the work function of oxidized copper is expected to be slightly higher.[26] Therefore, assuming no dynamical acceleration due to the laser field, the maximum energy of a photoelectron produced by a 7.9-eV photon would be 3.7 eV. Because the minimum electron energy required to cause molecular elimination from a neutral excited state of water ice is 6 eV,[25] photoelectrons from the substrate are unlikely to produce $O(^3P_J)$. In addition, the similar TOF spectra for 1 and 50 L exposures shown in Figure 3 rule out the dominance of a process induced by photoelectrons from the substrate.

Because electrons and photons have different selection rules, only $O(^1D)$ is observed in the molecular elimination reaction (4) for vacuum-ultraviolet photodissociation of gas-phase water:[27]

$$H_2O + h\nu \rightarrow H_2 + O(^1D). \quad (4)$$

In the condensed phase with 7.9-eV photons, reaction (4) leads to $O(^1D)$ desorption with $T_{trans}$ = 800 K.[12] Quenching of these $O(^1D)$ atoms to the ground state is improbable because $O(^1D)$ readily reacts with $H_2O$ to form $H_2O_2$ or 2 OH.[28]

In the condensed phase, conservation of momentum can involve neighboring water molecules, state mixing can occur due to many-body interactions, and ionization energies can be lowered considerably relative to the gas phase. It is therefore possible that $O(^3P_J)$ forms during photoexcitation by a molecular elimination step from a state very similar to that formed by direct inelastic electron scattering.[25] In this case, spin constraints are overcome by 7.9-eV photoionization of water (5) followed by ion-electron recombination (6). This triplet water can subsequently dissociate according to reaction (7):

$$H_2O + h\nu \rightarrow H_2O^+ + e^-, \quad (5)$$

$$H_2O^+ + e^- \rightarrow H_2O^*, \quad (6)$$

$$H_2O^* \rightarrow H_2 + O(^3P_J). \quad (7)$$

Although ionization of water ice at 7.9 eV has a low quantum yield (~2%) compared to 9.3 eV (22%), the amount of $O(^3P_J)$ formed as a result of reactions (5)–(7) may be significant compared to secondary mechanisms involving OH radicals. $O(^3P_J)$ formed in this manner is likely part of the

400 K component, as the energy corresponding to this component's peak (70 meV) is close to the energy reported for electron-stimulated desorption of $O(^3P_J)$ from $D_2O$ ice (60 meV).[25]

### B. Formation of $O(^3P_J)$ atoms through hydroxyl recombination reactions

$H_2O$ photodissociation at 157 nm can also be described by the following equation:

$$H_2O(ads) + h\upsilon(157\ nm) \rightarrow H(i) + OH(i),\ E_{avail} = 2.22\ eV, \quad (8)$$

where "i" stands for the vacuum/ASW interface and "ads" stands for adsorbed.[11] Following photodissociation according to reaction (8), recombination of two hydroxyls can produce either $H_2O_2$ or $O(^3P_J)$ and water. Further photodissociation of $H_2O_2$ can form two energetic hydroxyl groups.[12] Since the $O(^3P_J)$ TOF spectra from $H_2O$ and $H_2O_2$ appeared to be the same shape,[11] the hydroxyl recombination reactions involved in each case are likely similar. Four different exothermic recombination reactions of hydroxyls may be responsible for the observed $O(^3P_J)$ signal:

$$OH(i) + OH(i) \rightarrow H_2O(i) + O(^3P_J), \quad (9)$$

$$OH(i) + OH(i) \rightarrow H_2O(ads) + O(^3P_J), \quad (10)$$

$$OH(i) + OH(ads) \rightarrow H_2O(i) + O(^3P_J), \quad (11)$$

$$OH(i) + OH(ads) \rightarrow H_2O(ads) + O(^3P_J). \quad (12)$$

Enthalpies for these reactions are $\Delta_r H(9) = -0.73$ eV, $\Delta_r H(10) = -1.19$ eV, $\Delta_r H(11) = -0.17$ eV, and $\Delta_r H(12) = -0.63$ eV.[11]

Reactions (9) and (12) are close in energy and may both contribute to the observed "1800 K" component. The temperature of this component was actually allowed to vary between 1600 and 2000 K in order to get the best fit for each TOF spectrum. The peak position seemed to change with increasing irradiation and with excimer laser energy. If the "1800 K" component results from two separate mechanisms, the behavior of this component can be rationalized. Reaction (9) involves two OH(i) fragments, so it should require two photon excitations in close temporal and spatial proximity. Reaction (12) involves one OH(i) and one OH(ads), which is localized on the surface, so reaction (12) should only require one photon once a substantial number of hydroxyls have accumulated. The oxygen yield from reaction (9) should have a quadratic dependence on excimer energy, while the oxygen yield from reaction (12) should have a strong dependence on irradiation time and a linear dependence on excimer energy after significant irradiation. Therefore, it is not surprising that different peak positions were observed at different excimer energies and after differing amounts of irradiation. Because these two reactions have such similar energies, their Maxwell-Boltzmann distributions are convoluted, and both are contained in the "1800 K" component.

As already discussed in Sec. IV A, the 400 K component may be due in part to molecular elimination following ion-electron recombination. Reaction (11) may also contribute to this component, as it is less exothermic than reactions (9) and (12). As shown in Figure 8, the 400 K component increases with increasing irradiation. Reaction (11) involves an adsorbed hydroxyl group, so a buildup of hydroxyls due to increasing irradiation enhances the $O(^3P_J)$ signal from reaction (11).

In addition to atomic oxygen, recombination reactions (9) and (11) produce interfacial water molecules, which may desorb with significant vibrational excitation. Consequently, the irradiation time dependence of this oxygen signal should be similar to that of vibrationally excited water. In our previous work, the desorption yield of $H_2O$ ($\upsilon^*$) was found to increase with irradiation time.[9] While the irradiation time dependences of oxygen atoms produced specifically by reactions (9) and (11) could not be measured, the $O(^3P_J)$ signals at all flight times probed did increase with irradiation time.

### C. Thermal and diffusion components

Any time $O(^3P_J)$ is formed with an initial trajectory toward the surface, it may equilibrate with the surface and emerge with a translational temperature of 82 K, the surface temperature. As indicated in Table I, both the thermal and diffusion components are much larger for J = 2 than for J = 1 or 0. When $O(^3P_{J=1\ or\ 0})$ thermalizes with the surface, it may also lose internal energy and fall to the ground state, where J = 2.

Although oxygen atom diffusion occurs at temperatures as low as 40–50 K,[29] atomic oxygen desorption at 82 K is not necessarily immediate. Physisorbed oxygen atoms desorb thermally with a time constant determined by the Polanyi-Wigner equation:

$$\frac{-d\theta}{dt} = \upsilon\theta(t)^n e\frac{-E_{des}}{k_B T}, \quad (13)$$

where $\theta$ is the surface coverage (in layers or number of molecules), $\upsilon$ is the frequency factor (standard value $\sim 10^{12}$ $s^{-1}$), $n$ is the reaction order, $T$ is the surface temperature, and $E_{des}/k_B$ is the desorption energy divided by the Boltzmann constant. For atomic oxygen, $E_{des}/k_B$ has not been measured on ASW, but it was found to be 1455 K on graphite and 1764 K on amorphous silicates ($n = 1$ in both cases).[29,30] The time constant of oxygen atom desorption at 82 K depends significantly on the value of $E_{des}/k_B$ chosen. For example, 90% of the atoms desorb in 4.7 $\mu$s if $E_{des}/k_B = 1455$ K, but it takes 32 $\mu$s for 90% of the atoms to desorb if $E_{des}/k_B = 1764$ K. Since we do not know the actual desorption energy of oxygen atoms from ASW, it is difficult to calculate how much of the observed slower-than-thermal signal may be merely delayed thermal desorption as opposed to diffusion from within the bulk ice. Experimentally, the importance of thermal desorption should be possible to determine because the time constant of thermal desorption becomes shorter as the surface temperature rises. While we did not vary the surface temperature in the present experiments, for 50 L $H_2O$ exposure on a different substrate, we found that increasing

the surface temperature caused the amount of sub-thermal signal to rise and did not affect its flight time.[31] Although delayed thermal desorption was not the primary cause of the sub-thermal signal at 50 L exposure, it could be more important than diffusion at low coverages.

No diffusion component was discussed in the similar study by Hama *et al.*, even though their experimental data appeared to exceed the sum of the Maxwell-Boltzmann components at long flight times.[11] Because the TOF spectra we measured had similar shapes for 5 L, 50 L, and 600 L, with the exception of growing thermal and diffusion components, we would expect even larger thermal and diffusion components to be present at 1500 L exposure. The thermal and diffusion components may arise from all mechanisms proposed above as well as from direct photodissociation of hydroxyl groups.

### D. Formation of O($^3$P$_J$) atoms through photodissociation of adsorbed hydroxyls

As shown in Figure 8, the 10 000 K component is almost non-existent from freshly dosed ASW, but its signal increases rapidly with irradiation. Although none of the hydroxyl recombination reactions produce enough energy for a 10 000 K component, the photodissociation of adsorbed hydroxyls has more than enough available energy:

$$\mathrm{OH(ads)} + h\nu(157\ \mathrm{nm}) \rightarrow \mathrm{H(i\ or\ ads)} + \mathrm{O(^3P_J)}. \quad (14)$$

Reaction (14) has 2.85 eV available for H(i) or 3.03 eV available for H(ads).[11] In the gas phase, the majority of that available energy would be expected to go to the lighter H fragment, but, since the hydroxyl is adsorbed on the surface, the partitioning of energy may depend in large part on the hydroxyl's orientation. When oxygen is pointed away from the surface, the hydrogen's initial trajectory is toward the surface. After photodissociation, the hydrogen fragment may rebound off the surface and collide with the oxygen fragment. In this scenario, much of the hydrogen's rebounded kinetic energy is transferred to the oxygen. A Maxwell-Boltzmann temperature of 10 000 K corresponds to ∼1.8 eV. For H(i) in reaction (14), 1.8 eV corresponds to 63% of the total available energy. When the hydroxyl orientation is reversed, with H pointing away from the surface, the oxygen fragment collides with the surface and becomes part of the thermal component. A theoretical investigation of isolated OH radicals estimates the cross section for reaction (14) at 157 nm to be $3 \times 10^{-18}$ cm$^2$.[32,33] Therefore, after prolonged irradiation of ASW causes accumulation of surface hydroxyls, direct photodissociation of OH should contribute significantly to the observed O($^3$P$_J$) yield.

Because we measured TOF spectra at very low coverages and determined the precise value of $r$ by setting the thermal component equal to the surface temperature of 82 K, we are confident that the fastest component has $T_{trans} = 10\,000 \pm 2000$ K. The peak of this component is clearly defined in Figures 4 and 5. Figures 6 and 7 show that this component was almost unnecessary for freshly dosed ASW. Like Hama *et al.*,[11] we observed a large increase in the fastest component after prior irradiation, so we attributed this component to the photodissociation of OH radicals.

### E. Implications for outer solar system

The E ring of Saturn is dominated by tiny water ice particles, which are replenished primarily by geysers on Enceladus.[34] When these particles are exposed to UV photons, the water may dissociate and produce O($^3$P$_J$) by the mechanisms discussed above. We can use our measured cross sections for O($^3$P$_J$) depletion to estimate the lifetime of a typical water ice particle in the E-ring due to photodissociation. This simple model is merely intended to illustrate how the measured cross section may be applied. More advanced models will of course include many other loss terms, as the icy grains are also expected to experience sputtering by a plasma in the magnetosphere.[35]

From Cassini's Imaging Science Subsystem, the median radius of E-ring particles has been determined to be 3.1 $\mu$m.[36] The density of ASW formed at ∼100 K is 0.94 g cm$^{-3}$, which corresponds to $3.1 \times 10^{22}$ molecules cm$^{-3}$. The surface density is $1.2 \times 10^{15}$ molecules cm$^{-2}$ ($\eta$). Many water molecules on the surface of the ice particles in the E ring are photodissociated. For simplicity, we will consider the total number of OH and $H_2O$ molecules (N) in a spherical ice particle rather than distinguishing between these rapidly interconverting species. We will use the cross section from 5 L ASW, $\sigma = 6.5 \times 10^{-20}$ cm$^2$, since the E-ring grains have multilayer ice. The solar photon flux near Saturn between 150 and 160 nm is $7.5 \times 10^8$ photons cm$^{-2}$ s$^{-1}$ ($F_{ph}$).[37] The rate of O($^3$P$_J$) desorption, or hydroxyl depletion, due to photons in this wavelength range can then be calculated according to the following equation:

$$\frac{dN}{dt} = -F_{ph}\,\sigma\,\eta\,A(t), \quad (15)$$

where A(t) is the surface area of the sphere at time t. This equation assumes that only the molecules on the surface can desorb, but acknowledges that all molecules in the sphere will eventually be on the surface. Because the surface area changes with time, this equation was solved iteratively. The resulting decrease in radius with time is nearly linear with a rate of 0.57 Å/year for a grain with an initial radius of 3.1 $\mu$m. The radius reaches half of its initial value in about $2.7 \times 10^6$ years.

Since the cross section in this calculation did not include $H_2O$ photodesorption or direct photodissociation to produce O($^1$D), H, or OH, typical water ice particles in the E ring would be photo-destroyed in much less time. The total water removal/destruction cross section for 5 L ASW, which includes both photodesorption and photodissociation, was previously measured to be $\sim 9.5 \times 10^{-20}$ cm$^2$ at 157 nm.[9] With this cross section in Eq. (15), the radius would reach half of its initial value in about $2.2 \times 10^6$ years. Additional space weathering processes that contribute to destroying the ice particles more quickly include bombardment by micrometeoroids, electrons, protons, other charged particles, and photons with wavelengths below 150 nm. The relevant fluxes of these particles in the outer solar system can be found in a recent review article.[38]

These results imply that photodissociation of ice grains in the E-ring region of Saturn may contribute O($^3$P$_J$) to the atomic oxygen cloud and that the observed oxygen-atom

density near Saturn is not due solely to gas-phase processes. Since there is a replenishing source term for the ice grains related to geyser activity on Enceladus, the atomic oxygen density likely arises in part from condensed-phase processes occurring on these grains.

## V. CONCLUSION

Photodissociation of amorphous solid water deposited on a thinly oxidized copper substrate at 82 K was studied by measuring $O(^3P_{J=2,1,0})$ photoproducts detected with resonance-enhanced multiphoton ionization. For each spin-orbit state, the oxygen atom TOF spectrum was measured as a function of $H_2O$ exposure and 157-nm irradiation time. Four Maxwell-Boltzmann distributions with translational temperatures of 10 000 K, 1800 K, 400 K, and 82 K were required to fit the data. The most likely formation mechanisms are molecular elimination following ionization of water and ion-electron recombination, secondary recombination of hydroxyl radicals, and photodissociation of adsorbed hydroxyl radicals. Evidence for O-atom diffusion through bulk ASW was found for $H_2O$ exposures of at least 5 L. The cross sections for $O(^3P_2)$ depletion were $1.3 \times 10^{-19}$ and $6.5 \times 10^{-20}$ cm$^2$ for 1 and 5 L, respectively. Given the known photon fluxes and grain sizes, the calculated cross sections and lifetimes imply that photodissociation of ice grains in the E-ring region of Saturn may contribute $O(^3P_J)$ to the atomic oxygen cloud.

## ACKNOWLEDGMENTS

This work was supported by the NASA ROSES Outer Planets Program under Contract No. NNX10AB03G. The authors also acknowledge Dr. Gregory Grieves for useful discussions.

[1]Y. Futaana, J. Y. Chaufray, H. T. Smith, P. Garnier, H. Lichtenegger, M. Delva, H. Groller, and A. Mura, Space Sci. Rev. **162**(1–4), 213–266 (2011).
[2]H. T. Smith, R. E. Johnson, M. E. Perry, D. G. Mitchell, R. L. McNutt, and D. T. Young, J. Geophys. Res.: Space Phys. **115**, A10252 (2010).
[3]W. L. Tseng and W. H. Ip, Icarus **212**(1), 294–299 (2011).
[4]D. E. Shemansky, P. Matheson, D. T. Hall, H. Y. Hu, and T. M. Tripp, Nature (London) **363**(6427), 329–331 (1993).
[5]H. Melin, D. E. Shemansky, and X. M. Liu, Planet. Space Sci. **57**(14–15), 1743–1753 (2009).
[6]T. A. Cassidy and R. E. Johnson, Icarus **209**(2), 696–703 (2010).
[7]A. J. Farmer, Icarus **202**(1), 280–286 (2009).
[8]S. Kempf, U. Beckmann, G. Moragas-Klostermeyer, F. Postberg, R. Srama, T. Economou, J. Schmidt, F. Spahn, and E. Grün, Icarus **193**(2), 420–437 (2008).
[9]A. J. DeSimone, V. D. Crowell, C. D. Sherrill, and T. M. Orlando, J. Chem. Phys. **139**(16), 164702 (2013).
[10]A. Acocella, G. A. Jones, and F. Zerbetto, J. Phys. Chem. Lett. **3**, 3610–3615 (2012).
[11]T. Hama, A. Yabushita, M. Yokoyama, M. Kawasaki, and N. Watanabe, J. Chem. Phys. **131**(11), 114511 (2009).
[12]T. Hama, A. Yabushita, M. Yokoyama, M. Kawasaki, and N. Watanabe, J. Chem. Phys. **131**(11), 114510 (2009).
[13]T. Hama, A. Yabushita, M. Yokoyama, M. Kawasaki, and S. Andersson, J. Chem. Phys. **131**(5), 054508 (2009).
[14]S. Andersson, A. Al-Halabi, G. J. Kroes, and E. F. van Dishoeck, J. Chem. Phys. **124**(6), 064715 (2006).
[15]S. Andersson, G. J. Kroes, and E. F. van Dishoeck, Chem. Phys. Lett. **408**(4–6), 415–421 (2005).
[16]O. Votava, D. F. Plusquellic, and D. J. Nesbitt, J. Chem. Phys. **110**(17), 8564–8576 (1999).
[17]K. I. Oberg, H. Linnartz, R. Visser, and E. F. van Dishoeck, Astrophys. J. **693**(2), 1209–1218 (2009).
[18]M. S. Westley, R. A. Baragiola, R. E. Johnson, and G. A. Baratta, Nature (London) **373**(6513), 405–407 (1995).
[19]K. P. Stevenson, G. A. Kimmel, Z. Dohnalek, R. S. Smith, and B. D. Kay, Science **283**(5407), 1505–1507 (1999).
[20]M. A. Henderson, Surf. Sci. Rep. **46**(1–8), 1–308 (2002).
[21]S. Warren, W. R. Flavell, A. G. Thomas, J. Hollingworth, P. M. Dunwoody, S. Downes, and C. K. Chen, Surf. Sci. **436**(1–3), 1–8 (1999).
[22]D. F. Cox and K. H. Schulz, Surf. Sci. **256**(1–2), 67–76 (1991).
[23]Y. Matsumi, N. Shafer, K. Tonokura, M. Kawasaki, Y. L. Huang, and R. J. Gordon, J. Chem. Phys. **95**(10), 7311–7316 (1991).
[24]F. M. Zimmermann and W. Ho, Surf. Sci. Rep. **22**(4–6), 127–247 (1995).
[25]G. A. Kimmel and T. M. Orlando, Phys. Rev. Lett. **75**(13), 2606–2609 (1995).
[26]H. Kawano, Prog. Surf. Sci. **83**(1–2), 1–165 (2008).
[27]L. J. Stief, W. A. Payne, and R. B. Klemm, J. Chem. Phys. **62**(10), 4000–4008 (1975).
[28]W. Zheng, D. Jewitt, and R. I. Kaiser, Phys. Chem. Chem. Phys. **9**(20), 2556–2563 (2007).
[29]J. He, D. Jing, and G. Vidali, Phys. Chem. Chem. Phys. **16**(8), 3493–3500 (2014).
[30]M. D. Ward and S. D. Price, Astrophys. J. **741**(2), 121 (2011).
[31]A. J. DeSimone and T. M. Orlando, "Photodissociation of water and $O(^3P_J)$ formation on a lunar impact melt breccia," J. Geophys. Res.: Planets (to be published).
[32]E. F. Vandishoeck, S. R. Langhoff, and A. Dalgarno, J. Chem. Phys. **78**(7), 4552–4561 (1983).
[33]E. F. Vandishoeck and A. Dalgarno, J. Chem. Phys. **79**(2), 873–888 (1983).
[34]F. Postberg, S. Kemp, J. K. Hillier, R. Srama, S. F. Green, N. McBride, and E. Grun, Icarus **193**(2), 438–454 (2008).
[35]R. E. Johnson, M. Fama, M. Liu, R. A. Baragiola, E. C. Sittler, and H. T. Smith, Planet. Space Sci. **56**(9), 1238–1243 (2008).
[36]A. P. Ingersoll and S. P. Ewald, Icarus **216**(2), 492–506 (2011).
[37]A. S. Jursa, *Handbook of Geophysics and the Space Environment*, 4th ed. (Air Force Geophysics Laboratory, Hanscom AFB, MA, 1985).
[38]C. J. Bennett, C. Pirim, and T. M. Orlando, Chem. Rev. **113**(12), 9086 (2013).